INSTITUTE OF PHYSICS PUBLISHING JOURNAL OF PHYSICS B: ATOMIC, MOLECULAR AND OPTICAL PHYSICS

J. Phys. B: At. Mol. Opt. Phys. **38** (2005) 615–633 doi:10.1088/0953-4075/38/6/001

Photo double ionization of helium 100 eV and 450 eV above threshold: I. Linearly polarized light

A Knapp[1], A Kheifets[2], I Bray[3], Th Weber[1,5,6], A L Landers[4], S Schössler[1], T Jahnke[1], J Nickles[1], S Kammer[1], O Jagutzki[1], L Ph H Schmidt[1], M Schöffler[1], T Osipov[5,6], M H Prior[6], H Schmidt-Böcking[1], C L Cocke[5] and R Dörner[1]

[1] Institut für Kernphysik, Universität Frankfurt, August-Euler-Str. 6, D-60486 Frankfurt, Germany
[2] Research School of Physical Sciences and Engineering, Australian National University, Canberra, ACT 0200, Australia
[3] Centre for Atomic, Molecular and Surface Physics, Murdoch University, Perth, 6150, Australia
[4] Physics Department, Auburn University, Auburn, AL 36849, USA
[5] Department of Physics, Kansas State University, Cardwell Hall, Manhattan, KS 66506, USA
[6] Lawrence Berkeley National Lab, Berkeley, CA 94720, USA

E-mail: doerner@atom.uni-frankfurt.de

Received 30 November 2004, in final form 25 January 2005
Published 7 March 2005
Online at stacks.iop.org/JPhysB/38/615

Abstract

We present a joint experimental and theoretical study for the fully differential cross section of the photo double ionization (PDI) of helium with linearly polarized light at the excess energies $E_{\mathrm{exc}} = 100$ eV and 450 eV above the threshold. The fully differential cross section is obtained by measuring the three-dimensional momentum vectors of one electron and the He^{2+} ion in coincidence using the COLTRIMS method. We give an overview of the momentum distribution of the three-body continuum 100 eV above the threshold. We show angular distributions for both electrons for various energy sharings at $E_{\mathrm{exc}} = 100$ eV and 450 eV. The experimental results are well reproduced by a set of convergent close-coupling (CCC) calculations.

1. Introduction

The emission of two electrons from a helium atom after absorption of a single photon is a fundamental three-body process in atomic physics (for review articles, see [1] and [2]). It is characterized by the $^1S^e$ symmetry of the initial state which leads, within the dipole approximation [3], to the $^1P^o$ final state. There are also no resonant states in the three-body continuum above the double ionization threshold of 79 eV. It is also worth mentioning that contrary to multi-photon double ionization [4] the emission of both electrons after

absorption of one photon is a non-sequential process; because both electrons leave the atom at the 'same' time, electron repulsion certainly plays a major role in this dynamical process.

The main studies of PDI are focused on understanding the mechanisms of the reaction. This is best achieved by a complete dynamic characterization of the process that displays the complete momenta of all particles in the final state. The final state is defined by its angular momentum, parity and the nine momentum components of the two photoelectrons and the residual ion. The energy and momentum conservation reduces this number to five linearly independent components. Accordingly, the fivefold differential cross section (5DCS) $\mathrm{d}^3\sigma/(\mathrm{d}\Omega_1\mathrm{d}\Omega_2\mathrm{d}E_1) = \mathrm{d}^5\sigma/(\mathrm{d}E_1 \sin\Theta_1\mathrm{d}\Theta_1 \sin\Theta_2\mathrm{d}\Theta_2\mathrm{d}\Phi_1\mathrm{d}\Phi_2) = \mathrm{d}^5\sigma/(\mathrm{d}E_1\mathrm{d}\cos\Theta_1\mathrm{d}\cos\Theta_2\mathrm{d}\Phi_1\mathrm{d}\Phi_2)$ describes the final state dynamics. Here Θ_1, Θ_2 and Φ_1, Φ_2 are the polar and azimuthal emission angles with respect to the polarization axis of the electrons e_1 and e_2, respectively, and E_1 is the energy of the electron e_1.

In our experiment, we measured the momentum vectors of one electron and the doubly charged He^{2+} ion; thus we have determined six momentum components. The redundancy of six, versus the required five, components, permits valuable cross checks of the data. Within the dipole approximation the fivefold is reduced to a fourfold differential cross section (4DCS) $\mathrm{d}^4\sigma/(\mathrm{d}E_1\mathrm{d}\cos\Theta_1\mathrm{d}\cos\Theta_2\mathrm{d}\Phi_{12})$. This 4DCS contains all the information about the final state and hence is a fully differential cross section for this process.

Before the first coincident PDI experiments became feasible, the ratio of the total double to total single photo ionization cross sections was often measured. In the limit of large photon energies, where the shake-off mechanism is believed to be dominant [5], information about the electron correlation in the initial state could be gained from such experiments. In their pioneering coincident PDI experiment Schwarzkopf *et al* [6] measured the emission angles and the energies of both electrons at $E_{\mathrm{exc}} = 20$ eV with $E_1 = E_2 = 10$ eV (equal energy sharing). Since then impressive experimental and theoretical progress has been made. Up to now, the fivefold differential cross section of the PDI of helium has been investigated for different energy sharings by many experimental groups. These studies can be loosely grouped in three energy regions: first, near the double ionization threshold, where the electron dynamics can be understood by the Wannier theory [7–9]); second, in the middle energy region ($E_{\mathrm{exc}} = 2$–100 eV) where the double ionization is dominated by electron–electron scattering (4DCS are available from [7, 8, 10–22]). And third, for the high-energy region where shake-off plays a major role in the double ionization, only one measurement of the 4DCS at $E_{\mathrm{exc}} = 450$ eV has been reported so far [23].

In the present and companion papers immediately following this one, we report detailed studies of the PDI of He with linearly and circularly polarized light at excess energies of 100 eV and 450 eV. Our goal was to obtain the most consistent set of data across a wide photon energy range and to provide stringent tests of theoretical descriptions of the double ionization process. In addition to 4DCS, we also analyse our data in terms of the PDI amplitudes which contain the most intimate information on electron correlations.

The present paper begins our presentations by reporting the 4DCS for helium with linearly polarized light at the energies $E_{\mathrm{exc}} = 100$ eV and 450 eV above the double ionization threshold. We present the angular distributions of one electron, for various energy sharings, while the other electron's momentum is fixed at selected angles with respect to the polarization axis. In our companion paper II the 4DCS of PDI with circularly polarized light at $E_{\mathrm{exc}} = 100$ eV and 450 eV are reported. In that work we determined the circular dichroism (CD), i.e., the difference between the 4DCS for left and right circularly polarized light; this was done with $E_{\mathrm{exc}} = 100$ eV and 450 eV and for various energy sharing partitions between the two electrons. Paper III presents the symmetrized gerade and ungerade amplitudes extracted from the He

PDI measurements; these quantities are the fundamental parameters for the description of the PDI process.

The present paper is organized as follows. In section 2 we give a brief description of our experimental set-up. Section 3 outlines the convergent close-coupling (CCC) theory and in section 4 we present our results for various energy sharings. Atomic units are used throughout unless specified otherwise.

2. Experimental set-up

The experiment was performed at the beamline 4.0.2 [24] of the Advanced Light Source at the Lawrence Berkeley National Laboratory with the COLTRIMS technique (see [25] for a general review and [8, 26] for application to synchrotron radiation). The PDI is investigated at two different photon energies $E_\gamma = 179$ eV and $E_\gamma = 529$ eV with linearly polarized light. With the double ionization threshold at 79 eV, these photons impart excess energies of 100 eV and 450 eV, respectively.

In brief, the photon beam is focused into a supersonic helium gas jet. Electrons of energy below 60 eV are directed and guided by a combination of electric and magnetic fields onto a large area position sensitive channel plate detector[7]. From its time-of-flight and position of impact the momentum vector of the electron is deduced [27]. The electric field guides the ions with 4π collection solid angle for all momenta onto a second position sensitive detector, which has a diameter of 80 mm. The ion charge state and momentum vector are again obtained from the time-of-flight and the position of impact. The momentum vector of the fast electron is calculated from the measured slow electron and the recoiling ion using momentum conservation.

Figure 1 shows a sketch of the COLTRIMS chamber consisting of a double stage source chamber with two skimmers, a reaction chamber and a jet catcher where the helium jet is dumped. The supersonic jet enters the reaction chamber in which the spectrometer and the two position sensitive channel plate detectors (one at each end of the spectrometer) are located. The target region is located at the intersection of the spectrometer axis and the atomic beam axis. The jet terminates and is pumped away in the jet catcher above the spectrometer.

The supersonic gas jet is created in the double stage source chamber. The helium gas expands adiabatically into the first stage through a 30 μm diameter nozzle at a pressure around 13 bar. The first stage is evacuated by a 1000 ℓ s^{-1} turbomolecular pump. The jet goes through the second stage into the reaction chamber. Skimmers of 0.3 mm and 1 mm diameter are used for the first and second stage. This geometry yields a width of 1.3 mm for the jet at the interaction point. The target density in the intersection region (about 0.5 mm^3) is about 1×10^{11} cm^{-2}. The use of a second stage provides differential pumping to suppress the warm He gas in the reaction chamber. The jet is not pre-cooled. It has a speed ratio of about 30 resulting in a momentum uncertainty of less than 0.3 au parallel and less than 0.17 au perpendicular to the jet direction.

The spectrometer system used to obtain the momenta of one electron and the recoiling ion utilizes parallel electric and magnetic fields aligned along its axis (see figure 1). The total length is 831 mm and consists of two parts, one arm for the electrons (the distance from the target region to electron detector is 192 mm, hereafter called electron spectrometer), and another for the helium ions (the distance from the target region to recoiling ion detector is 639 mm, hereafter called recoiling ion spectrometer). The constant homogeneous magnetic field is produced by a Helmholtz coil pair [27].

[7] See Roentdek.com for details of the detectors.

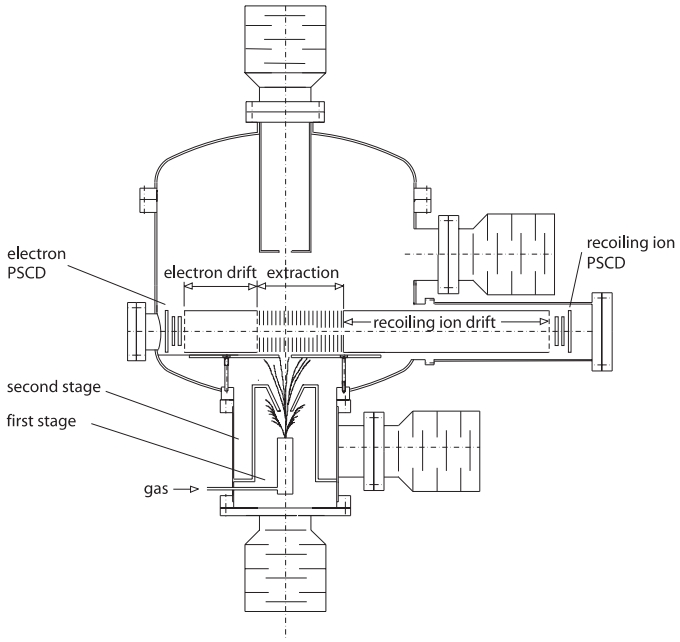

Figure 1. COLTRIMS jet assembly and chamber. The supersonic jet is produced in the double stage source chambers (bottom) and enters in the reaction chamber, goes through the spectrometer and is dumped in the jet catcher (top). The reaction zone lies in the intersection between the spectrometer axis and the jet (the photon beam would be out of the plane at the same intersection). The spectrometer is subjected to an electric and magnetic field. The magnetic field is parallel to the spectrometer axis and is produced by a Helmholtz coil pair which is not shown. The electric fields can be separated into an extraction field, an electrostatic lens on the recoiling ion side, and field-free drift regions on both the electron and recoiling ion sides. At each end of the spectrometer there is a position sensitive channel plate detector (PSCD) for the electron and the helium ions, respectively. Typical pressures are 3×10^{-4} mbar the source first stage, 1×10^{-7} mbar at the reaction chamber and 3.5×10^{-7} mbar at the jet catcher.

The electrostatic ion spectrometer consists of a homogeneous extracting field, followed by an electrostatic lens and a quasifield-free drift region. (The drift tube is separated from the recoiling ion detector by a woven mesh of 0.25 mm width.) This field distribution is essential for a good momentum resolution. Without the lens recoiling ions with the same momentum but different starting points within the overlap region of gas jet and photon beam would result in different trajectories with different times-of-flight and positions of impact. This would significantly degrade the recoiling ion momenta resolution. Figure 2 shows a simulation of the imaging characteristics of our spectrometer: all trajectories are from doubly charged helium ions starting with 3 au momentum in z-direction (the z-direction is parallel to the spectrometer axis). Even though they start from different positions at the same time, they are focused to a single point on the detector, again at the same time. This behaviour is reached by choosing a special field distribution in the following way. The target zone lies in a constant homogeneous field of 7.61 V cm^{-1}. After 89 mm the recoiling ions pass through an electrostatic lens. After the lens the recoiling ions enter a quasi field-free drift tube with the ion detector at its end. This field configuration yields a focus of the ions to a single point in time and space on the channel plate detector.

The electron spectrometer had the same extraction field of 7.61 V cm^{-1} as the ion spectrometer (since they overlap, this is unavoidable unless pulsed fields are used). After 63 mm of a constant homogeneous extraction field the electrons enter a 129 mm long

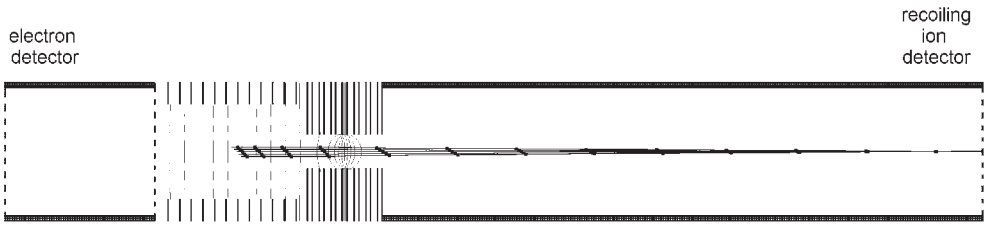

Figure 2. Simulation of the electric spectrometer with potential lines (thin dashed lines); Characteristics of time and space focusing, distance between the time markers (full squares) is 0.5 μs, ions start with 3 au in horizontal direction from a reaction volume of 8 mm × 8 mm × 8 mm. They are focused to a point of 0.6 mm × 0.6 mm, the time difference at the end of the quasi drift tube is less than 0.5 ns. The electric field in the target zone is 7.6 V cm^{-1}. The thick dashed lines illustrate the 0.25 mm width mesh.

field-free drift region. By choosing the drift length twice as long as the extraction length (Wiley–MacLaren geometry [28]), electrons starting at different distances arrive at the same time (through first order in small variations of the distance). Additionally, a magnetic field of 13 G is superimposed parallel to the electric field. This allows collection, with 4π solid angle efficiency, and sufficient energy resolution, of all electrons with energies up to 60 eV.

The times-of-flight of the electrons and the He^{2+} ions relative to the bunch marker (a pulse provided by the ALS, and synchronized to the 32 ps long photon pulses from the synchrotron) are used to calculate the momentum in offline analysis.

The calculation of the momenta of the He^{2+} ions is straightforward. Because of their heavy mass, the helium ions move much slower than the electrons and their interaction with the magnetic field is small and can be corrected easily. To first order, it is equivalent to a slight rotation of the ion detector. Also, the difference in times-of-flight between the He^{2+} ions leaving the interaction region with a finite momentum $T_{He^{2+}}(p_z)$ and those with zero axial momentum $T_{He^{2+}}(p_z = 0)$ is directly proportional to p_z.

Momentum measurement for electrons is more complicated. Because of the low mass, the electrons are guided on cyclotron trajectories. The momentum component parallel to the electric field depends only on the electric field and can be determined from the resulting time-of-flight. The other two momentum components perpendicular to the field are obtained from the position of impact on the detector, the time-of-flight T and the magnetic field B [27]:

$$p_{e_\perp} = \frac{qB\sqrt{\Delta x_e^2 + \Delta y_e^2}}{2|\sin(\omega_{gyr}T/2)|} \tag{1}$$

where $\Delta x_e = x_e - x_{0e}$ and $\Delta y_e = y_e - y_{0e}$; x_e, y_e represent the true position of impact and x_{0e}, y_{0e} are the position of impact corresponding to that of an electron with zero momentum in x- and y-direction. B is the magnetic field, q is the electric charge and ω_{gyr} is the gyration frequency. The magnetic field B is obtained from the data itself. If the distance $\sqrt{\Delta x_e^2 + \Delta y_e^2}$ versus the time-of-flight is plotted, one gets a structure shown in figure 3. The time between nodes (where the distance is zero) is the cyclotron gyration period from which the magnetic field can be easily calculated. But this wiggle structure also has a disadvantage. Whenever electrons perform an integer number of complete turns they hit the detector at the projection of their starting point (x_{0e}, y_{0e}), independent of their initial transverse momentum. For those flight times the information of the electron transverse momentum is lost. Those events are discarded in the data analysis. In our experiment, this effect does not lead to blind regions in the phase space. This is so because for linear polarized light with polarization parallel to the spectrometer axis z and for circular polarized light there is a reflection symmetry with

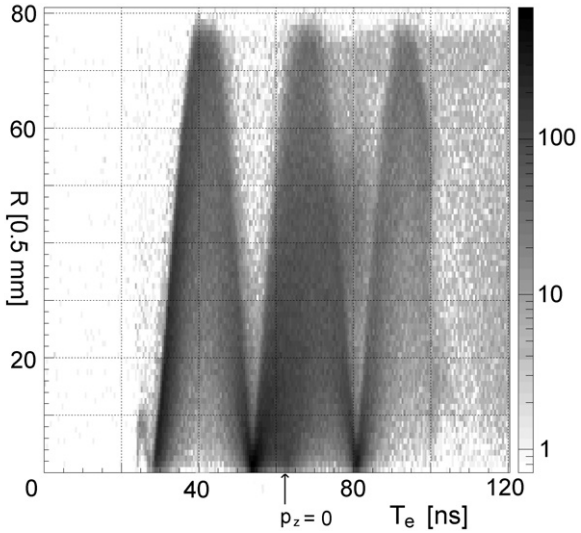

Figure 3. Distance R of the electron position (in units of 0.5 mm) of impact versus the electron time-of-flight T_e in ns, logarithmic scale. The magnetic field is 13 G which can be deduced from the time distance of two nodes equal to the time length of one turn. The gyration period depends solely on the magnetic field and is independent of the electric field. The arrow marks the time-of-flight of an electron which starts with zero momentum ($p_z = 0$ au).

respect to the xy plane. Therefore, the electric field is chosen in a way that the position of the nodes is asymmetric around T_{0e}. This has the advantage that the nodes can be filled up in the following way: if there is a node at $p_{z_e} = c_1$ with a corresponding z-momentum for the He^{2+} ion $p_{z_{He^{2+}}} = c_2$ one can replace it by the mirrored momenta $p_{z_e} = -c_1$ and $p_{z_{He^{2+}}} = -c_2$.

Figure 3 shows the distance of the position of impact of the electron relative to (x_{0e}, y_{0e}) versus the time-of-flight in corresponding channels. The distance between the two nodes is about 26 ns. The position of the nodes relative to T_{0e} is asymmetric to T_{0e}. In every figure showing the 4DCS the nodes have been filled up exploiting this mirror symmetry.

Measuring the full 3D momenta of one electron and the recoiling ion makes our data set overcomplete. We have determined six momentum components of which only five are linearly independent. After calculating the full momentum of one electron and the He^{2+} ion the full three-dimensional vector momentum of the complementary electron can be deduced. To cross check the data we plot the energy of one electron e_1 versus the energy of the complementary one e_2 (figure 4). All real coincidence events are located in the diagonal given by $E_1 = E_\gamma - 79\,\text{eV} - E_2$. The width of the diagonal line shows the overall resolution of our spectrometer.

We normalized our data in two different ways. For the data at $E_{exc} = 100$ eV, one of the electrons always fulfils the condition $E_1 \leqslant 50$ eV. The 4π detection for all electrons up to 50 eV and a constant efficiency of the electron detector independent of the electron energy allow coverage of the full final state phase space. Therefore we can normalize the 100 eV data to the very precisely measured total double ionization cross sections by Samson *et al* [29, 30]. This normalization is straightforward: the absolute number of coincident counts for $E_1 \leqslant 50$ eV is equivalent to the absolute double ionization cross section of 2.8 kbarn.

Because of our restricted electron detection above 60 eV we cannot use the same normalization for the $E_{exc} = 450$ eV data. Here, we normalized the experimental data to the CCC calculation. The number of all total coincidence counts with $E_1 \leqslant 60$ eV is

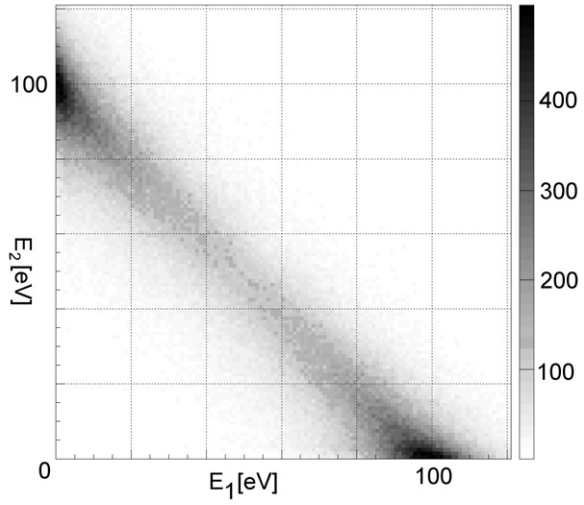

Figure 4. Energy distribution e_1 versus e_2 for 100 eV above the threshold. The sum of both electron energies is 100 eV.

equivalent to the integration of the single differential ionization cross section from 0 eV to 60 eV $\int_{0\,\mathrm{eV}}^{60\,\mathrm{eV}} (\mathrm{d}\sigma/\mathrm{d}E_1)\,\mathrm{d}E_1$.

3. CCC calculations

In the CCC formalism, we describe the final state with two electrons in the continuum $\Psi(\boldsymbol{k}_1, \boldsymbol{k}_2)$ by a close-coupling expansion on the basis of channel functions. Each channel function is a product of a $Z = 1$ Coulomb wave of energy $k_1^2/2$ and a positive energy target pseudostate of energy $k_2^2/2$. The latter are determined by diagonalization of the target Hamiltonian utilizing an orthogonal Laguerre basis. We increase the size of the basis until convergence to a desired precision is obtained. Hence the method is named convergent close-coupling (CCC). The helium atom ground state Ψ_0 is described by a 20-term Hylleraas expansion which recovers more than 99.98% of the correlation energy. A highly accurate description of the initial state is necessary to obtain essentially gauge-independent results.

We calculate the fully differential cross section of the PDI on He as a squared dipole matrix element between the correlated ground state and the CCC final state with the two electrons in the continuum:

$$\frac{\mathrm{d}^3\sigma_{M_P}}{\mathrm{d}\Omega_1\,\mathrm{d}\Omega_2\,\mathrm{d}E_1} = C|\langle\Psi(\boldsymbol{k}_1, \boldsymbol{k}_2)|\mathrm{d}_{M_P}|\Psi_0\rangle|^2. \tag{2}$$

Here the dipole operator d_{M_P} depends on the polarization of light and the gauge of the electromagnetic interaction. In the case of the linearly polarized light and the length gauge, $d_{M_P=0} = z_1 + z_2$. In this case, the proportionality constant in (2) is $C = 4\pi^2 E_\gamma/c$. Alternatively, the dipole operator in the velocity gauge $\partial/\partial z_1 + \partial/\partial z_2$ or the acceleration gauge $2/z_1^3 + 2/z_2^3$ can be chosen. In the case of the circularly polarized light, the combination $d_{M_P=0} \pm d_{M_P=1}$ should be taken in equation (2) with the sign depending on helicity.

We use a partial wave expansion and introduce bipolar harmonics in equation (2),

$$\langle\Psi(\boldsymbol{k}_1, \boldsymbol{k}_2)|d_{M_P}|\Psi_0\rangle = \sum_{JM}\sum_{l_1 l_2} \mathcal{Y}_{JM}^{l_1 l_2}(\hat{k}_1, \hat{k}_2) D_{l_1 l_2}(E_1 E_2)(-1)^{M_P}\delta_{M_P+M,0} \tag{3}$$

where $\mathcal{Y}_{JM}^{l_1 l_2}(\hat{k}_1, \hat{k}_2) = \sum_{m_1 m_2} C^{JM}_{l_1 m_2, l_2 m_2} Y_{l_1 m_1}(\hat{k}_1) Y_{l_2 m_2}(\hat{k}_2)$ [31].

The reduced dipole matrix element is defined by the following projection,

$$D_{l_1 l_2}(E_1, E_2) = \langle \Psi_{l_l n_2 l_2}(k_1) \| D_{M_P} \| \Psi_0 \rangle \langle l_2 k_2 \parallel l_2 n_2 \rangle, \tag{4}$$

where $\langle l_2 k_2 \parallel l_2 n_2 \rangle$ is the radial overlap between the pseudostate of energy $\epsilon_{n_2 l_2} = E_2 = k_2^2/2$ and the true $Z = 2$ continuum radial wavefunction of same energy and angular momentum. The matrix elements $\langle \Psi_{l_l n_2 l_2}(k_1) \| D_{M_P} \| \Psi_0 \rangle$ are found by solving a coupled set of integral Lippmann–Schwinger equations. This asymmetric treatment of both electrons goes to the core of the CCC method and is explained in detail in [32]. Following [33], the basis sizes are taken to be $N_{l_2} = N_0 - l_2$ with a constant (independent of l_2) Laguerre exponential fall-off parameter λ. This yields $\epsilon_{n_2 l_2}$ that are different for each l_2. In order to obtain the required partial amplitudes at the experimentally specified E_2 energy, for each l_2, we interpolate the amplitudes available at the discrete energies $\epsilon_{n_2 l_2}$. The process of interpolation takes into account the step-function behaviour of the CCC amplitudes. Subsequently, a single CCC calculation yields results for all possible energy sharings, and depends on only two parameters N_0 and λ. For a given angular momenta expansion, convergence is then tested by, say, keeping λ constant and increasing N_0. At 100 eV, where energy sharing ranges from symmetric to asymmetric, we found sufficient convergence by taking $N_0 = 40$ and $\lambda = 3.8$. Not all of the generate states were included in the close-coupling expansion, only the open and the lowest three closed, a total of around $30 - l_2$ states for each l_2. At 450 eV, where only highly asymmetric energy sharing is being considered, we included all states generated with $N_0 = 20$ and $\lambda = 2.4$.

The bipolar harmonics entering equation (5) can be evaluated by using the following expression [34],

$$\mathcal{Y}_{1M}^{l_1 l_2}(\hat{k}_1, \hat{k}_2) = -\frac{1}{4\pi} \left(\frac{3}{l_{\max}} \right)^{1/2} [(-1)^{l_1} P'_{l_1}(\cos\theta_{12})(\hat{k}_1)_M + (-1)^{l_2} P'_{l_2}(\cos\theta_{12})(\hat{k}_2)_M], \tag{5}$$

where $\cos\theta_{12} = (\hat{k}_1 \cdot \hat{k}_2)$. This allows us to write the dipole matrix element as

$$\langle \Psi(\boldsymbol{k}_1, \boldsymbol{k}_2) | d_{M_p=0} | \Psi_0 \rangle = \big(k_{1z} + k_{2z}\big) a_{\mathrm{g}} + \big(k_{1z} - k_{2z}\big) a_{\mathrm{u}}. \tag{6}$$

An analogous expression with $M_P = 1$ contains k_{1x} and k_{2x}. Here we introduced the symmetric (gerade) and antisymmetric (ungerade) DPI amplitudes,

$$a_{\substack{\mathrm{g} \\ \mathrm{u}}} = \frac{\sqrt{3}}{4\pi} \sum_{l=0}^{\infty} \frac{(-1)^l}{\sqrt{l+1}} [P'_{l+1}(\cos\theta_{12}) \mp P'_l(\cos\theta_{12})] D^{\pm}_{ll+1}(E_1, E_2), \tag{7}$$

calculated via symmetric and antisymmetric combinations of the reduced dipole matrix elements, respectively,

$$D^{\pm}_{l_1 l_2}(E_1, E_2) = \tfrac{1}{2}\{D_{l_1 l_2}(E_1, E_2) \pm D_{l_1 l_2}(E_2, E_1)\}. \tag{8}$$

4. Results

First, we will present an overview of the three particle kinematics in the final state continuum for $E_{\mathrm{exc}} = 100$ eV. For a closer inspection we will show thereafter the 4DCS for $E_{\mathrm{exc}} = 100$ eV and $E_{\mathrm{exc}} = 450$ eV in the common polar and azimuthal angles for various energy sharings. Additionally, the angular distributions will be discussed in detail with respect to the selection rules and explained in terms of the parametrization of the transition matrix element suggested by Huetz *et al* [35] and Malegat *et al* [36].

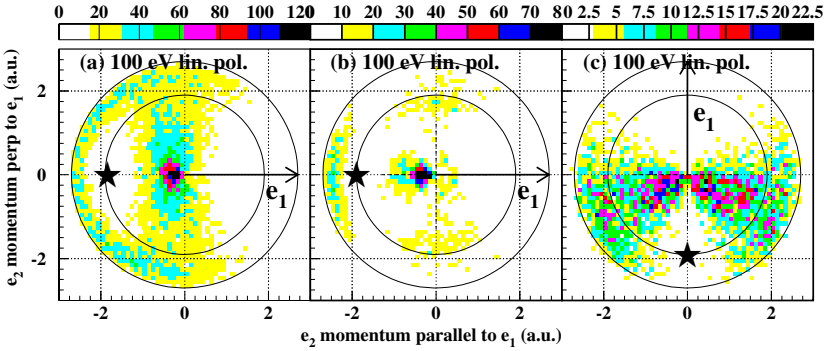

Figure 5. Momentum distribution of the second electron e_2 with respect to the first electron e_1 for $E_{exc} = 100$ eV above the threshold. The two electrons are in a plane perpendicular to the light propagation x: $\Theta_{x1} = \Theta_{x2} = 90^\circ \pm 30^\circ$, where Θ_x is the polar angle with respect to the light propagation. The arrow indicates the direction of the first electron e_1. The outer circle is the maximum possible momentum. The inner circle indicates the locus of events with equal energy sharing. Panel (a) is integrated over all orientations of the polarization axis, while (b) and (c) show subsamples of all events shown in (a). The polarization vector in (b) and (c) is horizontal. (b) electron e_1 is parallel within $\Theta_1 = \pm 30^\circ$ (Θ refers to the polar angle with respect to the polarization axis) to the polarization axis; (c) electron e_1 is perpendicular to the polarization axis, $\Theta_1 = 90^\circ \pm 5^\circ$ to the polarization axis. The star marks the location of the node at $\boldsymbol{p}_1 = -\boldsymbol{p}_2$ (selection rule C). This node is independent of the polarization and is therefore present in all three panels. In panel (c) selection rule A is visible, which forbids emission of both electrons perpendicular to the polarization vector.

(This figure is in colour only in the electronic version)

4.1. Overview

An overview of the three particle dynamics in the final state for $E_{exc} = 100$ eV is given in figure 5. The density plot shows the momentum distribution for electron e_2 for fixed direction of electron e_1 indicated by the arrow. Both electrons are chosen to be perpendicular to the light propagation. The outer circle indicates the locus where electron e_2 has all the excess energy of 100 eV, the inner circle shows the locus where both electrons have 50 eV energy. This illustration makes use of the advantages of a COLTRIMS apparatus: on the one hand, collecting the charged particles in the full solid angle, on the other hand, no pre-selection of the energy sharings. In figure 5(a) integration over all orientations of the polarization vector is performed. Figures 5(b) and (c) are subsets of figure 5(a). In figure 5(b) and (c) the angle between e_1 and the polarization vector is fixed and the polarization axis in both panels is horizontal. In figure 5(b) the fixed electron e_1 is parallel to the polarization axis; in figure 5(c) the fixed electron e_1 is perpendicular to the polarization axis.

In figure 5 the structure of the observed momentum distribution is dominated by two physical effects. Due to electron repulsion both electrons are mainly emitted to opposite half spheres. The second major effect is the final state symmetry $^1P^o$. Maulbetsch and Briggs [37] have derived the geometries where the final state wavefunction has a node. Two selection rules can be seen in figure 5 classified according to the nomenclature of Maulbetsch and Briggs. All three panels show a node marked by the star at $\boldsymbol{p}_1 = -\boldsymbol{p}_2$. The initial ground state of helium has a positive parity which turns into the negative parity of the final state after absorption of the photon. This negative parity for $\boldsymbol{p}_1 = -\boldsymbol{p}_2$ requires that the wavefunction is identically zero at this point (selection rule C). This node is independent of the polarization and is therefore present in all three panels.

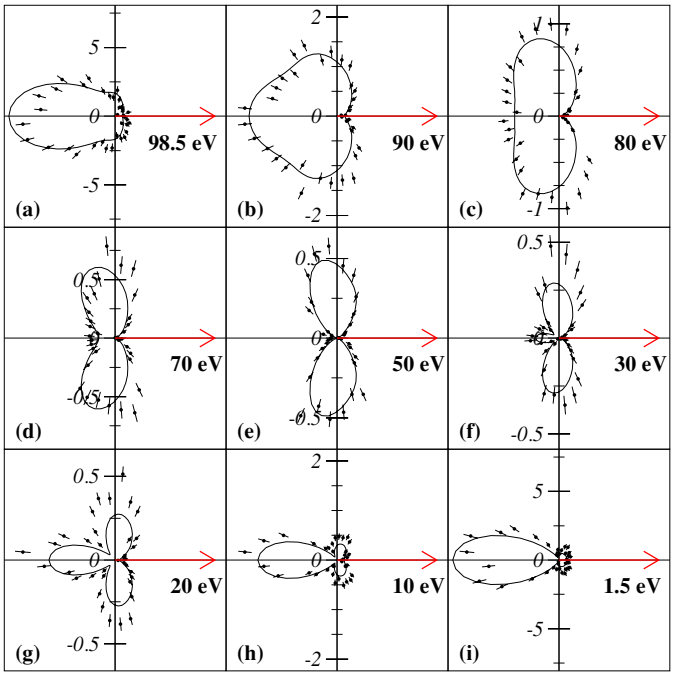

Figure 6. Fourfold differential cross section of the He PDI at $E_\gamma = 179$ eV photon energy on absolute scale in barn/(eVrad). In all panels the polarization axis is horizontal. The direction and the energy of one of the two electrons is fixed as indicated by the number and the arrow. E_1 is always the energy of the fixed electron. The polar plots show the angular distribution of the complementary electron, which is within $\pm$ 5° (a), (b), (d), (f), (h), (i) and $\pm$ 10° (c), (e), (g) in the plane. The solid line is a full CCC calculation in velocity gauge. The measurements are normalized to precisely measured total cross section by Samson *et al* [29, 30]. Note the change in scale between the panels. (a) $97 < E_1 < 100$ eV, $-5^\circ < \Theta_1 < 5^\circ$; (b) $85 < E_1 < 95$ eV, $-5^\circ < \Theta_1 < 5^\circ$; (c) $75 < E_1 < 85$ eV, $-5^\circ < \Theta_1 < 5^\circ$; (d) $65 < E_1 < 75$ eV, $-5^\circ < \Theta_1 < 5^\circ$; (e) $45 < E_1 < 55$ eV, $-5^\circ < \Theta_1 < 5^\circ$; (f) $25 < E_1 < 35$ eV, $-5^\circ < \Theta_1 < 5^\circ$; (g) $25 < E_1 < 35$ eV, $-5^\circ < \Theta_1 < 5^\circ$; (h) $5 < E_1 < 15$ eV, $-5^\circ < \Theta_1 < 5^\circ$; (i) $0 < E_1 < 3$ eV, $-5^\circ < \Theta_1 < 5^\circ$.

Selection rule A can be found in panel (c). The cross section vanishes if both electrons are emitted 90° to the polarization vector. This selection rule is a consequence of the transition from the $^1S^e$ state into a $^1P^o$ state. If both electrons are emitted 90° to the polarization vector the final state with the total angular momentum $L = 1$ and its projection onto the polarization axis $M = 0$ has a node. This selection rule holds for all energy sharings. .

4.2. 4DCS 100 eV above threshold

For a closer inspection and a more thorough comparison with theory, the 4DCS are presented in figures 6–11 for different energy sharings. We show the 4DCS on an absolute scale and in the common polar and azimuthal angles for coplanar geometry, i.e., both electrons and the polarization vector are in the plane of paper. The solid line in each panel is the CCC calculation in the velocity gauge. Length and acceleration guage results would be barely distinguishable from those using the velocity gauge and are not shown. Figures 6–11 show how the 4DCS depend on the energy sharing. For $E_{\rm exc} = 100$ eV data in figures 6–8 we have chosen five different energy sharings, four unequal and one equal energy sharing: 1.5 eV $\leftrightarrow$ 98.5 eV;

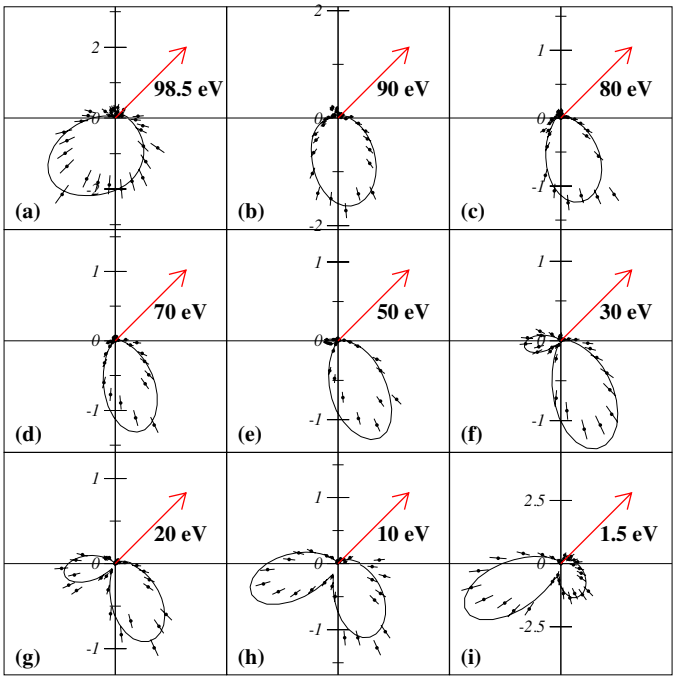

Figure 7. Same as in figure 6 except the angle between the polarization axis and the fixed electron is $\Theta_1 = (45 \pm 3)^\circ$, the complementary electron is within the plane defined by the polarization vector and the fixed electron within $\pm 15^\circ$.

10 eV $\leftrightarrow$ 90 eV; 20 eV $\leftrightarrow$ 80 eV; 30 eV $\leftrightarrow$ 70 eV and 50 eV $\leftrightarrow$ 50 eV. The angle between the fixed electron and the polarization vector is chosen to be $\Theta_1 = 0^\circ$, 45° and 90°.

In figure 6 the 4DCS for the fixed electron parallel to the polarization vector is shown. There is a strong dependence of the angular distribution on the energy sharing. The angular distribution of the very slow electron with the fast electron being fixed shows only one lobe, but different shapes (figures 6(a)–(c)): the angular distribution of the slow electron looks like an ellipse (figure 6(a)), while the distribution for a slightly higher energy of the complementary electron E_2 is changed to the shape of a heart (figure 6(b)); this distribution is also called an apple by Schmidt *et al*. With increasing energy two lobes are formed (figures 6(d) and (e)). At equal energy sharing there is a node in the angular distribution (figure 6(e)). This is due to selection rule C: the cross section vanishes if $\boldsymbol{p}_1 = -\boldsymbol{p}_2$. Secondly, at equal energy sharing we find a node also for $\boldsymbol{p}_1 = \boldsymbol{p}_2$; the cross section is zero if both electrons are emitted into the same direction due to the electron repulsion. For $E_2 \geqslant 50$ eV a third lobe parallel to the polarization vector and on the opposite direction of the fixed electron emerges (figure 6(f)). With increasing energy of the complementary electron this third lobe grows relative to the other two lobes which are perpendicular to the polarization axis. These two lobes perpendicular to the polarization axis become only one lobe with more asymmetric energy sharings (figures 6(h) and (i)). So, finally, at an energy of 98.5 eV we find an angular distribution which consists again of two lobes parallel to the polarization axis, one much larger than the other (figure 6(i)). This angular distribution has the shape of a fish. The CCC calculation yields excellent agreement with the experiment in shape and in magnitude at all energy sharings.

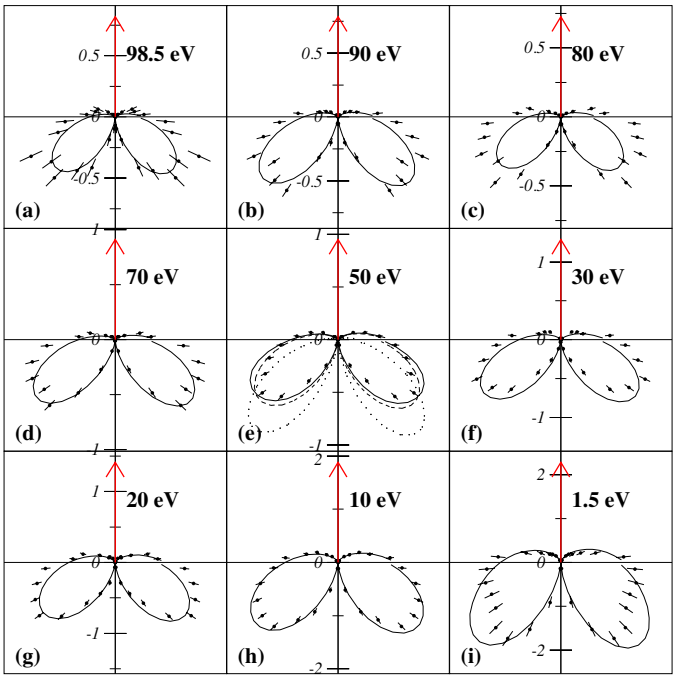

Figure 8. Same as in figures 6 and 7 except the angle between the polarization axis and the fixed electron is $\Theta_1 = (90 \pm 5)^\circ$, the complementary electron is within the plane defined by the polarization vector and the fixed electron within $\pm 15^\circ$. Dashed and dotted lines in (e) show the corresponding distribution for $E_{\mathrm{exc}} = 20$ eV and $E_{\mathrm{exc}} = 1$ eV (see the text).

At $\Theta_1 = 45^\circ$ (figure 7), the angular distribution looks significantly different from the previous ones (figure 6). For the distribution of the slow electron we find a more or less round structure which peaks around 200° to the polarization vector and 180° to the fixed electron (figure 7(a)). With increasing energy E_2 the lobe of the angular distribution gets narrower (figures 7(b) and (c)). At equal energy sharing (figure 7(e)) there are two lobes, a big (third and fourth quadrant) and a small one (parallel to the polarization vector). With increasing E_2 the small lobe in the second and third quadrants grows in relation to the other one (figures 7(f)–(i)). At an energy of $E_1 = 10$ eV for the fixed electron the two lobes have nearly the same magnitude (figure 7(h)). Comparing the number of lobes in the angular distribution for $\Theta_1 = 0^\circ$ and $\Theta_1 = 45^\circ$ we observe differences: figures 6(f) and (g) show clearly three lobes, while in figures 7(f) and (g) just two lobes are visible.

At $\Theta_1 = 90^\circ$ between the fixed electron and the polarization vector (figure 8) the angular distributions in all panels look quite the same as we expect from selection rule A. This selection rule and the node at the back-to-back emission of the electrons do not allow much 'freedom' for the angular distributions. In all panels there is a two lobe structure observed. For the case of equal energy sharing there are two additional angular distributions plotted (figure 8(e)). These lines correspond to the angular distribution of $E_1 = E_2 = 10$ eV (dashed line) and $E_1 = E_2 = 0.5$ eV (dotted line); both angular distributions are from [8]. These two lines and our experimental data for $E_1 = E_2 = 50$ eV differ in the angular position of the lobe maxima, their relative size and their width. The lobes of $E_1 = E_2 = 0.5$ eV and $E_1 = E_2 = 10$ eV are narrower than the lobes of the 50 eV electron. Additionally, the lobes are emitted more backwards to the electron with fixed emission direction. This behaviour as well as the angular

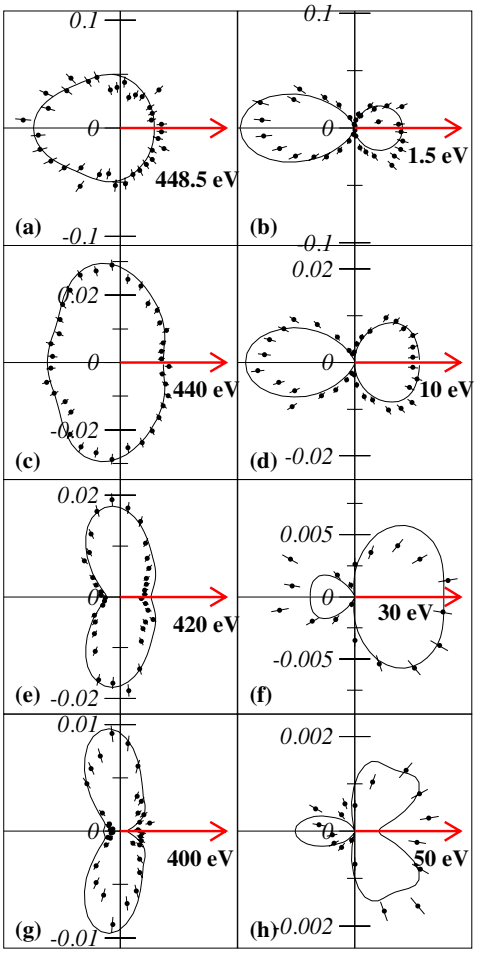

Figure 9. Fourfold differential cross section of the He PDI at 529 eV photon energy normalized to CCC calculation in barn/(eV rad). In all panels the polarization axis is horizontal. The direction and the energy of one of the two electrons is fixed as indicated by the number and the arrow. E_1 is always the energy of the fixed electron. The polar plots show the angular distribution of the complementary electron, which is in the plane within $\pm 20^\circ$(a), (b), (c), (d), (e), (f) and $\pm 25^\circ$(g), (h). The solid line is a full CCC calculation in velocity gauge. Panels (a), (b), (e) and (f) are from [23]. (a) $447 < E_1 < 500$ eV, $-25^\circ < \Theta_1 < 25^\circ$, (b) $0 < E_1 < 3$ eV, $-25^\circ < \Theta_1 < 25^\circ$, (c) $434 < E_1 < 446$ eV, $-25^\circ < \Theta_1 < 25^\circ$, (d) $4 < E_1 < 16$ eV, $-30^\circ < \Theta_1 < 30^\circ$, (e) $410 < E_1 < 430$ eV, $-25^\circ < \Theta_1 < 25^\circ$, (f) $20 < E_1 < 40$ eV, $-25^\circ < \Theta_1 < 25^\circ$, (g) $390 < E_1 < 410$ eV, $-30^\circ < \Theta_1 < 30^\circ$, (h) $40 < E_1 < 60$ eV, $-25^\circ < \Theta_1 < 25^\circ$.

distributions in general can be best explained by using the parametrization of the transition matrix element suggested by Huetz *et al* [35] and Malegat *et al* [36]. They have shown that the 5DCS can be separated within the dipole approximation into geometrical factors and dynamical parameters,

$$\frac{\mathrm{d}^5\sigma}{\mathrm{d}E_1 \mathrm{d}\cos\Theta_1 \mathrm{d}\cos\Theta_2\, \mathrm{d}\Phi_1 \mathrm{d}\Phi_2} = |a_\mathrm{g}(\cos\Theta_1 + \cos\Theta_2) + a_\mathrm{u}(\cos\Theta_1 - \cos\Theta_2)|^2. \tag{9}$$

(see also equation (6)). Here Θ_1 and Θ_2 are the angles of emission of the two electrons with respect to the polarization axis and Θ_{12} is the angle between the direction of both

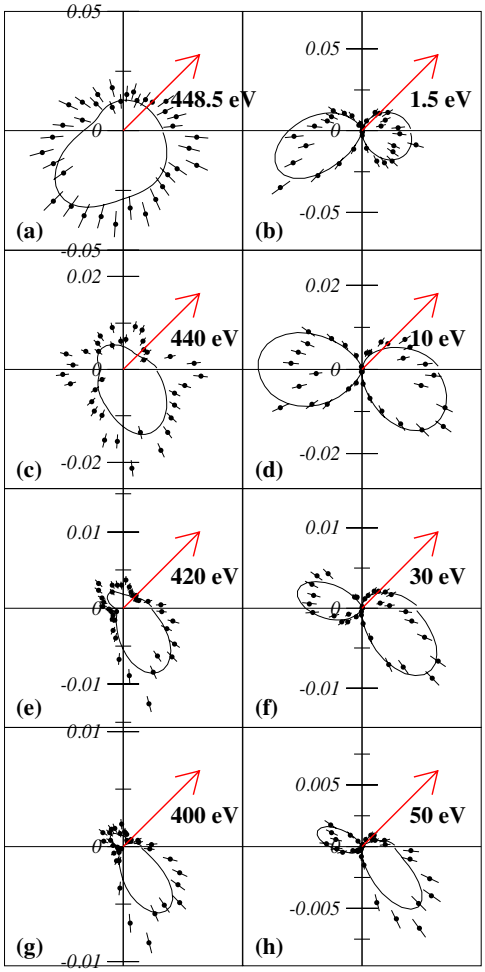

Figure 10. Same as in figure 9 except the angle between the polarization axis and the fixed electron is $\Theta_1 = (45 \pm 10)^\circ$, the complementary electron is within the plane defined by the polarization vector and the fixed electron within $\pm 25^\circ$.

electrons. The gerade (symmetric) and ungerade (antisymmetric) amplitudes a_g and a_u are complex functions of the electron energies E_1 and E_2 and their relative angle Θ_{12}. In equation (9) $(\cos\Theta_1 + \cos\Theta_2)$ and $(\cos\Theta_1 - \cos\Theta_2)$ are the geometrical factors reflecting the $^1P^o$ symmetry whereas a_g and a_u are dynamical parameters.

For equal energy sharing the ungerade amplitude vanishes and equation (9) reduces to a simpler form:

$$\left.\frac{d^5\sigma}{dE_1\, d\cos\Theta_1\, d\cos\Theta_2\, d\Phi_1\, d\Phi_2}\right|_{E_1=E_2} = |a_g|^2(\cos\Theta_1 + \cos\Theta_2)^2. \tag{10}$$

By measuring the 5DCS (10) the squared gerade amplitude $|a_g|^2$ can be obtained. Because of this simplicity many groups have extracted $|a_g|^2$ for equal energy sharing [6–8, 20, 38]. In the case of equal energy sharing, experimentally extracted squared amplitude $|a_g|^2$, also called the correlation factor, demonstrates a Gaussian shape which is predicted by the Wannier theory

$$|a_g|^2 \propto \exp\left[-4\ln 2(\pi - \Theta_{12})^2 / \Delta\Theta_{12}^2\right]. \tag{11}$$

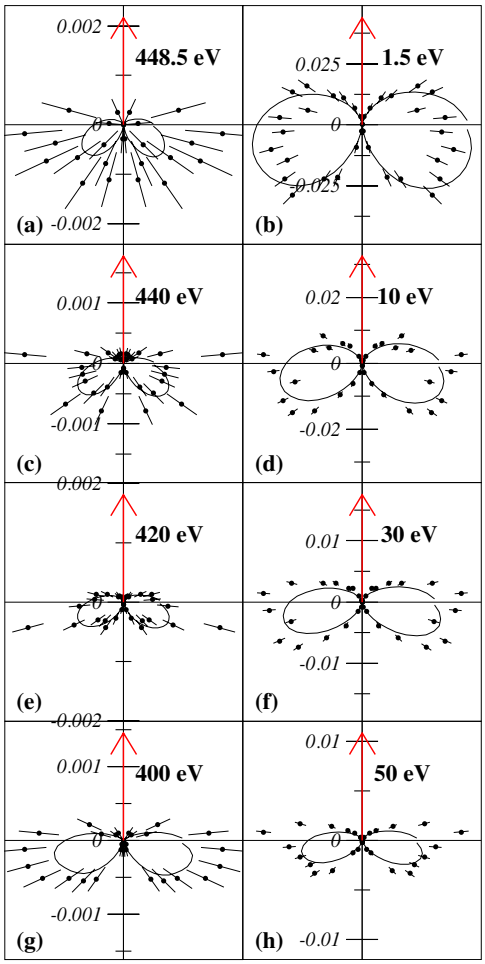

Figure 11. Same as in figures 9 and 10 except the angle between the polarization axis and the fixed electron is $\Theta_1 = (90 \pm 5)^\circ$, the complementary electron is within the plane defined by the polarization vector and the fixed electron within $\pm 25^\circ$.

Here the Gaussian width parameter $\Delta\Theta_{12}$ determines the full width at half maximum (FWHM) of the Θ_{12} distribution. The Gaussian width depends on the photon energy [35].

We fit the 4DCS for equal energy shown on panel (e) of figure 8 with the Gaussian ansatz (11) and obtained a FWHM of $121^\circ \pm 3^\circ$. For comparison, on the same panel we draw the 4DCS (10) with a Gaussian width FWHM = 68° ($E_{\rm exc} = 1$ eV [8]) and FWHM = 91° ($E_{\rm exc} = 20$ eV [8]) seen as dotted and dashed lines respectively. With a decreasing photon energy the lobes become narrower and more backward emitted. This is a result of the electron repulsion which plays an increasingly important role with decreasing excess energy.

To understand the angular distributions in the case of unequal energy sharing the ungerade amplitude has to be taken into account. Bolognesi *et al* have shown that $|a_{\rm u}|^2$ for an energy of 40 eV above the threshold and an energy sharing of 5 eV $\leftrightarrow$ 35 eV can be described by a Gaussian also [39]. If we treat $|a_{\rm u}|^2$ also for $E_{\rm exc} = 100$ eV as being more or less a Gaussian and the phase between both amplitudes to be independent of Θ_{12} (for a detailed study of

$|a_g|$, $|a_u|$ and the relative phase, see paper III), much can be learned by describing the angular distribution in terms of the gerade and ungerade amplitudes.

In figure 8 where the fixed electron is perpendicular to the polarization axis all angular distributions are similar because of two aspects. On the one hand, the shapes of the gerade and ungerade amplitudes are nearly the same. On the other hand, $+\cos^2\Theta_2$ and $-\cos^2\Theta_2$ terms both show a dipole distribution, i.e., they represent the same selection rule A. Therefore the small variations (angular positions of the lobe maxima, their relative sizes and their widths) are due to the different FWHM of the gerade and ungerade amplitudes and the ratio between the gerade and ungerade amplitudes for the different energy sharings.

To understand the angular distributions for unequal energy sharing and $\Theta_1 \neq 90^\circ$ a few more facts are relevant. The ratio $|a_g|^2/|a_u|^2$ drops with a decreasing E_1/E_2 (with $E_1 \leqslant E_2$), secondly, at the double ionization threshold, the ungerade amplitude is nearly zero. With increasing photon energy $|a_u|$ grows in relation to $|a_g|$. The angular distributions are an interplay between the gerade and the ungerade amplitudes which are weighted by the geometrical factors. At selected geometries or equal energy sharing the influence of each amplitude on the angular distributions is observable.

The angular distribution (ellipse) of the $E_2 = 1.5$ eV electron (figure 6(a)) is mainly due to the ungerade amplitude weighted by $(1 - \cos\Theta_2)^2$, which has its maximum at $\Theta_2 = \Theta_{12} = 180^\circ$. Additionally, the ungerade amplitude is maximal at an angle $\Theta_{12} = 180^\circ$ between both electrons (see also paper III). The gerade amplitude instead is weighted by $(1 + \cos\Theta_2)^2$ and has therefore a maximum at $\Theta_2 = \Theta_{12} = 0^\circ$; it is zero for $\Theta_2 = \Theta_{12} = 180^\circ$. Hence, the part of $|a_g|$ at $\Theta_{12} = 180^\circ$ is zero. The 5DCS at $\Theta_{12} = 180^\circ$ is defined by $|a_u|$:

$$5\mathrm{DCS}(E_1, E_2, \Theta_1 = 0^\circ, \Theta_{12} = 180^\circ) = 4|a_u(E_1, E_2, \Theta_{12} = 180^\circ)|^2. \qquad (12)$$

Therefore the angular distribution in figure 6(a) is due to mainly the ungerade amplitude. The same argument can be applied for figure 6(i). The distribution of the 98.5 eV electron has the shape of a fish. This structure can be divided into the main body of the fish (second and third quadrant) and into the fish fins which are perpendicular to the polarization axis. Its main body shape is mainly due to the ungerade amplitude. The fins, however, are a result of the gerade amplitude weighted with $(1 + \cos\Theta_2)^2$. The variations in the shapes of the angular distribution in figures 6(a) and 6(i) result from the fact that $|a_u|$ changes its sign with permutation of both electrons.

4.3. 4DCS 450 eV above threshold

After this overview of the 4DCS at $E_{exc} = 100$ eV we now discuss the 4DCS at a much higher energy of $E_{exc} = 450$ eV. Figures 9–11 show the 4DCS dependence on the energy sharing. We choose four different cases: 1.5 eV $\leftrightarrow$ 448.5 eV; 10 eV $\leftrightarrow$ 440 eV; 30 eV $\leftrightarrow$ 20 eV and 50 eV $\leftrightarrow$ 400 eV. The angle between the fixed electron and the polarization vector is again chosen to be 0°, 45° and 90°. We discuss the shape of the angular distributions in terms of the gerade and ungerade amplitudes.

First, the distribution of the fast electron will be discussed. At extreme asymmetric energy sharing we find a somewhat distorted dipole distribution for the fast electron (figures 9(b) and (d)). This can be taken as evidence that the fast electron is the one which primarily absorbs the photon energy as well as its angular momentum [23]. At low and intermediate photon energies an interpretation of the data in terms of a simple two-step mechanism where an electron absorbs the photon and successively the second electron is ejected by a shake-off [5], or knock out (TS1) [40, 41] mechanism, is complicated by the fact that it is unclear which of the two detected electrons is the primary photoelectron. Figures 9(b)

and (d) show that at higher excess energy of 450 eV this is changed and it seems well justified to speak about a primary and secondary electrons. At more symmetric energy sharing there are still two lobes parallel to the polarization vector, but surprisingly this time the lobe parallel to the fixed electron is much larger than the lobe antiparallel to the fixed electron (figure 9(f)). This should be compared to figures 6(h) and (i) where the lobe antiparallel to the fixed electron is much bigger than that parallel to the fixed electron. The reason is the following: as $5DCS_{180^\circ}$ depends solely on $|a_u|^2$ (equation (12)), the 5DCS for parallel emission is obtained by

$$5DCS(E_1, E_2, \Theta_1 = 0^\circ, \Theta_{12} = 0^\circ) = 4|a_g(E_1, E_2, \Theta_{12} = 0^\circ)|^2. \tag{13}$$

At intermediate excess energies both $|a_g|^2$ and $|a_u|^2$ show a Gaussian shape. $|a_u|^2$ at $\Theta_{12} = 180^\circ$ is always higher than $|a_g|^2$ at $\Theta_{12} = 0^\circ$. Therefore, the magnitude for antiparallel emission is higher than for parallel emission. The larger lobe for parallel emission simply means that $|a_g|^2$ at $\Theta_{12} = 0^\circ$ is larger than $|a_u|^2$ at $\Theta_{12} = 180^\circ$ at this energy sharing (see also the companion paper III).

For the slow electron there is a nearly isotropic distribution at extreme asymmetric energy sharing (figure 9(a)). At $E_1 = 440$ eV the distribution for the slow electron shows only a weakly structured ellipse (figure 9(c)). With more symmetric energy sharing, i.e., higher energy for the slow electron, we find emission of the slow electron into a narrow cone at 90° to the fast electron (figures 9(e) and (g)). One might think that this two-lobe structure—the narrow cone of 90° of the slow electron to the fast one—is a result of the same physics as in figures 6(d)–(f). In these figures the two-lobe structure arises from the selection rule C, which is valid at equal energy sharing. In terms of the parametrization by Huetz *et al* [35] and Malegat *et al* [36], the ungerade amplitude is exactly zero for equal energy sharing and nearly zero for almost equal energy sharing. Hence, only the gerade amplitude contributes to the angular distribution. Because the geometrical factor $(1 + \cos\Theta_2)^2$ is zero for back-to-back emission there is a two-lobe structure.

In contrast, figures 9(e) and (g) show the angular distribution for rather extreme asymmetric energy sharing. In this case, both amplitudes contribute to the angular distribution. Hence, the two-lobe structure in figures 9(e) and (g) is not comparable to the two-lobe structure in figure 6(d), (e) or (f). If the two-lobe structure does not arise from $|a_g|^2 \cdot (1 + \cos\Theta_2)^2$ the source of this pattern must be found in the shape of the amplitudes itself and therefore in the dynamics of the electrons.

Knapp *et al* [23] have argued that very low-energy secondary electrons are mostly emitted via the shake-off process [5] while higher energy transfer requires a hard binary (e,2e) collision [40, 41] and leads to an angle of 90° between the electrons. The signatures of both mechanisms can also be seen in figure 10.

In figure 10 the angle between the fixed electron and the polarization vector is $\Theta_1 = 45^\circ$. The angular distribution for the fast electron shows a dipole structure. Again, we find a more or less isotropic distribution with a slightly backward emission for the slow electron. For higher energy of the slow electron (figures 10(e) and (g)) we find a two-lobe structure for the angular distribution. Again, the two cones are 90° to the fast electron.

In figure 11 the angle between the fixed electron and the polarization vector is $\Theta_1 = 90^\circ$. Similarly, all angular distributions show a two-lobe structure due to the geometrical factors; for $E_2 = 30$ eV and $E_2 = 50$ eV due to geometrical factors and the dynamical parameters. The different dynamical parameters are responsible for the different appearance of the lobes: in figure 11(b) the lobes are wide and almost round, while the lobes in figures 11(e)–(h) have a far narrower structure.

In summary, we have presented here the experimental and theoretical 4DCS of the PDI of helium with linearly polarized light yielding excess energies of 100 eV and 450 eV above the

threshold. The CCC calculations yield excellent agreement with the experiment in shape and in absolute value at all energy sharings. For 100 eV above the threshold we have confirmed the selection rules derived by Maulbetsch and Briggs [37]. Comparing the angular distribution for equal energy sharing with that for $E_{\rm exc} = 20$ eV and $E_{\rm exc} = 1$ eV we find that the electron repulsion for a sum energy of 100 eV is less prominent than for 20 eV above the threshold. For 450 eV we see a dramatic change in the dynamics between both electrons for different energy sharings: there is an isotropic distribution for the slow electron with an energy of 1.5 eV; if the energy of the slow electron is slightly higher ($E_2 = 30$ eV and $E_2 = 50$ eV) we see emission of the slow electron into a narrow cone of 90° to the fast electron. This is not a result of selection rule C, but a result of the three-body Coulomb dynamics. This indicates that the two different double ionization mechanisms are active at different energy sharings.

Acknowledgments

This work was supported in part by BMBF, DFG, the Division of Chemical Sciences, Geosciences and Biosciences Division, Office of Basic Energy Sciences, Office of Science, US Department of Energy. A Knapp thanks Graduiertenförderung des Landes Hessen for financial support. ThW thanks Graduiertenfoerderung des Landes Hessen as well as the Alexander von Humboldt Foundation for financial support. We thank E Arenholz and T Young and the staff of the Advanced Light Source for extraordinary support during our beam time. The CCC computations presented in this paper were performed using the Compaq AlphaServer SC National Facility of the Australian Partnership for Advanced Computing.

References

[1] Briggs J and Schmidt V 2000 *J. Phys. B: At. Mol. Opt. Phys.* **33** R1
[2] Dörner R, Schmidt-Böcking H, Weber Th, Jahnke T, Schöffler M, Knapp A, Hattass M, Czasch A, Schmidt L Ph H and Jagutzki O 2004 *Radiat. Phys. Chem.* **70** 191–206
[3] Istomin A, Manakov N L, Meremianin A V and Starace A 2004 *Phys. Rev. Lett.* **92** 063002
[4] Dörner R, Weber Th, Weckenbrock M, Staudte A, Hattass M, Moshammer R, Ullrich J and Schmidt-Böcking H 2002 Multiple ionization in strong laser fields *Adv. At. Mol. Phys.* **48** 1–36
[5] Byron F W and Joachain C J 1967 *Phys. Rev.* **164** 1
[6] Schwarzkopf O, Krässig B, Elmiger J and Schmidt V 1993 *Phys. Rev. Lett.* **70** 3008
[7] Dawber G, Avaldi L, McConkey A G, Rojas H, MacDonald M A and King G C 1995 *J. Phys. B: At. Mol. Opt. Phys.* **28** L271
[8] Dörner R *et al* 1998 *Phys. Rev.* A **57** 1074
[9] Huetz A and Mazeau J 2000 *Phys. Rev. Lett.* **85** 530
[10] Achler M, Mergel V, Spielberger L, Azuma Y, Dörner R and Schmidt-Böcking H 2001 *J. Phys. B: At. Mol. Opt. Phys.* **34** 965
[11] Bolognesi P, Camelloni P, Coreno M, Turri G, Berakdar J, Kheifets A and Avaldi L 2001 *J. Phys. B: At. Mol. Opt. Phys.* **34** 3193
[12] Bräuning H P *et al* 1998 *J. Phys. B: At. Mol. Opt. Phys.* **31** 5149
[13] Cvejanovic S, Wightman J P, Reddish T J, Maulbetsch F, MacDonald M A, Kheifets A S and Bray I 2000 *J. Phys. B: At. Mol. Opt. Phys.* **33** 265
[14] Collins S A *et al* 2002 *Phys. Rev.* A **65** 052717
[15] Dawson C, Cvejanovic S, Seccombe D P, Reddish T J, Maulbetsch F, Huetz A, Mazeau J and Kheifets A S 2001 *J. Phys. B: At. Mol. Opt. Phys.* **34** L525
[16] Huetz A, Lablanquie P, Andric L, Selles P and Mazeau J 1994 *J. Phys. B: At. Mol. Opt. Phys.* **27** L13
[17] Knapp A *et al* 2002 *J. Phys. B: At. Mol. Opt. Phys.* **35** L521
[18] Lablanquie P, Mazeau J, Andric L, Selles P and Huetz A 1995 *Phys. Rev. Lett.* **74** 2192
[19] Schwarzkopf O and Schmidt V 1995 *J. Phys. B: At. Mol. Opt. Phys.* **28** 2847
[20] Turri G, Avaldi L, Bolognesi P, Camilloni R, Coreno M, Berakdar J, Kheifets A S and Stefani G 2002 *Phys. Rev.* A **65** 034702

[21] Viefhaus J, Avaldi L, Heiser F, Hentges R, Gessner O, Rüdel A, Wiedenhöft M, Wielczek K and Becker U 1996 *J. Phys. B: At. Mol. Opt. Phys.* **29** L729
[22] Wightman J P, Cvejanovic S and Reddish T J 1998 *J. Phys. B: At. Mol. Opt. Phys.* **31** 1753
[23] Knapp A *et al* 2002 *Phys. Rev. Lett.* **89** 033004
[24] Young A T *et al* 2001 *Nucl. Instrum. Methods* A **549** 467
[25] Dörner R, Mergel V, Jagutzki O, Spielberger L, Ullrich J, Moshammer R and Schmidt-Böcking H 2000 *Phys. Rep.* **330** 96–192
[26] Dörner R *et al* 1996 *Phys. Rev. Lett.* **77** 1024
Dörner R *et al* 1997 *Phys. Rev. Lett.* **78** 2031 (erratum)
[27] Moshammer R, Ullrich J, Unverzagt M, Schmitt W, Jardin P, Olson R E, Dörner R, Mergel V and Schmidt-Böcking H 1996 *Nucl. Instrum. Methods* B **107** 62
[28] Wiley W C and McLaren I H 1995 *Rev. Sci. Instrum.* **26** 1150
[29] Samson J A R, He Z X, Yin L and Haddad G N 1994 *J. Phys. B: At. Mol. Opt. Phys.* **27** 887
[30] Samson J A R, Stolte W C, He Z X, Cutler J N, Lu Y and Bartlett R J 1998 *Phys. Rev.* A **57** 1906
[31] Varshalovich D A 1988 *Quantum Theory of Angular Momentum* (Philadelphia: World Scientific)
[32] Kheifets A S and Bray I 1998 *J. Phys. B: At. Mol. Opt. Phys.* **31** L447
[33] Bray I 2002 *Phys. Rev. Lett.* **89** 273201
[34] Manakov N L, Marmo S I and Meremianin A V 1996 *J. Phys. B: At. Mol. Opt. Phys.* **29** 2711
[35] Huetz A, Selles P, Waymel D and Mazeau J 1991 *J. Phys. B: At. Mol. Opt. Phys.* **24** 1917
[36] Malegat L, Selles P and Huetz A 1997 *J. Phys. B: At. Mol. Opt. Phys.* **30** 251
[37] Maulbetsch F and Briggs J S 1995 *J. Phys. B: At. Mol. Opt. Phys.* **28** 551
[38] Schwarzkopf O and Schmidt V 1995 *J. Phys. B: At. Mol. Opt. Phys.* **28** 2847
[39] Bolognesi P, Kheifets A S, Bray I, Malegat L, Selles P, Kazansky A K and Avaldi L 2003 *J. Phys. B: At. Mol. Opt. Phys.* **36** L241
[40] Carlson T A 1967 *Phys. Rev* **156** 142
[41] Samson J A R 1990 *Phys. Rev. Lett.* **65** 2861